processes

MDPI

Article

Adaptive Modified Active Disturbance Rejection Control for the Superheated Steam Temperature System Under Wide Load Conditions

Huiyu Wang [1], Zihao Tong [2], Zhenlong Wu [2,3,4,*], Hongtao Zheng [3], Bing Li [5] and Yanfeng Jia [6]

[1] College of Chemistry and Chemical Engineering, Taiyuan University of Technology, Taiyuan 030024, China; huiyuwang86@gmail.com
[2] School of Electrical and Information Engineering, Zhengzhou University, Zhengzhou 450001, China; tongzihao@gs.zzu.edu.cn
[3] Shanxi Research Institute for Clean Energy, Tsinghua University, Taiyuan 030032, China; zhenghongtao@hsenergy.cn
[4] Huadian Zhengzhou Mechanical Design Institute Co., Ltd., Zhengzhou 450046, China
[5] Rundian Energy Science and Technology Co., Ltd., Zhengzhou 8450000, China; libing286@crpower.com.cn
[6] Sanmenxia Power Supply Co., State Grid Henan Electric Power Co., Sanmenxia 472000, China; jiayanfeng2@126.com
* Correspondence: wuzhenlong2020@zzu.edu.cn

Abstract

The operation of the superheated steam temperature system significantly impacts the safety and economy of thermal power units. To ensure its stable operation under large-scale variable load conditions, a modified active disturbance rejection control strategy based on parameter adaptation is proposed. Firstly, a typical superheated steam temperature system model is introduced, and the cascade control structure is applied to the model. Then, on this basis, a modified active disturbance rejection control strategy based on parameter adaptation is proposed, and the parameter tuning method of the modified active disturbance rejection control is introduced. Finally, the control performance of the proposed control strategy under a wide range of variable loads is verified through comparative simulations under nominal working conditions and uncertain working conditions. To further illustrate the effectiveness of the proposed strategy, the method is applied to a certain 660 MW unit in the field. After implementing the method, the fluctuation range of superheated steam temperature on the A and B sides decreased to only 34.0% and 53.0% of the original, respectively, and the fluctuation variance on the A and B sides decreased to only 28.5% and 43.3% of the original, respectively. The above field application results fully demonstrate that the control strategy proposed does not merely remain at the theoretical simulation level, but is a key technical means that can be effectively implemented and effectively solve the problem of superheated steam temperature control in thermal power units.

Keywords: superheated steam temperature system; modified active disturbance rejection control; parameter adaptation; cascade control; wide load; robustness

Check for updates

Academic Editors: Lefeng Cheng, Xiaoshun Zhang and Huaizhi Wang

Received: 8 December 2025
Revised: 12 January 2026
Accepted: 13 January 2026
Published: 15 January 2026

Copyright: © 2026 by the authors. Licensee MDPI, Basel, Switzerland. This article is an open access article distributed under the terms and conditions of the Creative Commons Attribution (CC BY) license.

1. Introduction

In recent years, more and more renewable energy is connected to the power grid. Due to its high sensitivity to environmental factors and inherent volatility, renewable energy causes large fluctuations in the power generation of the grid. To ensure stable grid

operation, thermal power units in traditional power systems need to perform deep peak shaving and frequency regulation to meet the flexibility requirements from large-scale renewable integration. However, rapid load changes can affect the stable operation of thermal units. During fast load variations and under various disturbances, key operating parameters such as main steam pressure, superheated steam temperature, and reheat steam temperature fluctuate significantly, which leads to reduced control performance. The superheated steam temperature (SST) system is a critical component of a thermal power unit [1]. If the SST is too high or too low, it can cause irreversible damage to the unit. Excessively high temperature may damage equipment, while excessively low temperature reduces efficiency. Therefore, maintaining good control of SST is crucial for the stability and safety of thermal power units [2].

To ensure the safe operation of the unit, it is necessary to control the fluctuation range of the SST as much as possible. Only when the fluctuation range is small enough can the set value be increased, which improves the economic performance of the unit. However, the operation of the SST involves processes such as steam superheating, combustion, and heat transfer. Its temperature change shows large inertia and long delay characteristics [3], which makes the control of the SST difficult to carry out.

To suppress temperature fluctuations in the SST during rapid load changes and under various disturbances, many researchers have carried out related studies. A multi-model dynamic matrix control strategy based on enthalpy prediction of the intermediate point is proposed to improve traditional PID control [4]. An accurate feedforward mechanism is introduced into a cascade control system to achieve better performance than traditional cascade control [5]. Based on sliding mode variable structure control, a new sliding mode control method is designed to outperform conventional cascade PID control [6]. In addition, a nonlinear control method is developed using a high-order sliding mode observer to suppress multiple types of disturbances [7]. With the development of artificial intelligence, many researchers have also tried to apply AI technology to the SST. To improve the control of strongly coupled and long-time-delay processes, a deep neural network-based identification method is proposed [8], which has strong generalization ability and stability for the system. A prediction model for the SST is built using machine learning, with model parameters optimized by a random search algorithm [9]. IIn order to accurately predict the changing trend of superheated steam temperature, a superheated steam temperature prediction model based on an improved whale algorithm optimizing long short-term memory neural network is proposed [10]. A neural network-based prediction model is used for the superheated steam temperature system, and a feedforward-feedback control strategy is adopted to improve control performance [11].

On the one hand, although PID control boasts advantages such as a simple structure, easy implementation, fast dynamic response, and strong robustness, it still has drawbacks, including poor adaptability, limited anti-disturbance capability, and insufficient ability to handle large time-delay processes when applied to nonlinear systems with significant inertia [12]. Therefore, it often needs to be combined with other control strategies to achieve effective control under complex working conditions. On the other hand, artificial intelligence technologies such as neural networks and reinforcement learning have strong nonlinear modeling capabilities and offer major advantages in predictive modeling and dynamic identification. However, during the implementation process, they require a large amount of training data to support them, which takes a considerable amount of time. There are still considerable challenges in practical applications.

In summary, the controller for the SST should have strong anti-disturbance ability, high robustness, and should not rely on an accurate model. Active disturbance rejection control (ADRC) is proposed by researcher Han Jingqing based on PID control and modern

control theory. It provides effective control for multi-input, multi-output and high-order systems, while also having a simple structure and strong robustness. ADRC combines the idea of eliminating errors based on errors in classical control theory and the idea of observing and compensating for errors through state observers in modern control theory. It can overcome the difficulties in solving nonlinear problems and the reliance on precise mathematical models. It regards various uncertainties in the controlled object, including internal and external disturbances, as total disturbances. It uses an extended state observer (ESO) to estimate and compensate for the total disturbances in real time, achieving active suppression and elimination of disturbances. In recent years, it has been applied in many fields. An ADRC is applied in a battery thermal management system, demonstrating excellent thermal stability [13]. An ADRC based on phase advance error is proposed and validated in an ultra-supercritical unit, showing excellent tracking and disturbance rejection performance [14]. To improve the performance of permanent magnet synchronous motor control systems, an ADRC strategy optimized by particle swarm optimization is introduced, which enhances system robustness and dynamic response speed [15]. For thermal power processes with large time-delay characteristics, Ref. [16] proposed a quantitative tuning rule for the time-delayed ADRC (TD-ADRC) structure based on the typical first-order plus time delay (FOPTD) model. Simulation and laboratory water tank experiments validated the tuning efficacy. Ref. [17] proposed a delay-inertia-compensation ADRC (DIC-ADRC) for time-delay dominant industrial systems, where these systems can be approximated as second-order plus time-delay (SOPTD) systems, and verified its robustness and control performance through on-site application in the main steam pressure process. An improved ADRC is proposed to accurately estimate the mover position and speed required by a permanent magnet synchronous linear motor system [18]. A modified ADRC based on gain scheduling is proposed and applied to the denitration system of a coal-fired unit, achieving better control performance [19]. In addition, an improved ADRC is presented for the SST along with its parameter tuning approach [20]. To improve the efficiency of wind energy conversion systems (WECS) equipped with permanent magnet synchronous generators (PMSG) under variable wind conditions, Ref. [21] enhanced the tracking performance and adaptive capability of the system by integrating ADRC with the perturb and observe (P&O) algorithm. Ref. [22] proposed an innovative solution combining an interleaved DC-DC boost converter with a nonlinear MPPT-ADRC strategy; the robust ADRC compensated for system disturbances and enhanced the stability of the hospital's power grid system under fluctuating solar radiation. To address the challenges associated with weak active disturbances, substantial steady-state speed amplitude fluctuations, and difficulty in achieving a balance between overshoot and speed control in the sensorless PMSM control system, Ref. [23] proposed a sensorless vector ADRC method for permanent magnet synchronous motors based on the Luenberger observer and proved that this control method has the advantages of small steady-state error and strong self-disturbance resistance through simulation experiments. Considering the renewable energy sources and energy storage, a scheme of load frequency control is proposed based on the deep deterministic policy gradient and ADRC for multi-region interconnected power systems [24]. Ref. [25] theoretically analyzes multiple types of ADRC and applies them to the main steam pressure system, demonstrating their potential for practical use. In addition, ADRC has also been widely used in other fields such as intelligent ship system [26], robotic systems [27,28], aircraft control systems [29], rehabilitation exercise control systems [30], distillation process [31], and permanent magnet motor drive systems [32]. It can be seen that the ADRC methods mentioned in these references are widely applied in complex nonlinear systems due to their low dependence on accurate models and strong robustness.

However, significant limitations still exist when the conventional ADRC is directly applied to systems with large inertia characteristics, such as the SST system of thermal power plants. Specifically, the SST system faces two core challenges: first, due to the large inertia characteristic of the system, the output will be delayed, resulting in the input signal of ESO being out of sync and thus unable to achieve precise observation and compensation of the system. Second, the current operating conditions of thermal power plants are subject to changes, requiring large-scale load adjustments.

To address the large inertia of the SST system, Han [12] proposed two key perspectives: the control signal compensation and output prediction. Based on these two perspectives, time-delay ADRC [33] and smith-predictor ADRC [34] have been proposed. Nevertheless, both methods suffer from output oscillations and degraded control performance when there is a mismatch in time delay [35]. To solve this problem, a modified active disturbance rejection control (MADRC) strategy is proposed [35]. However, in the context of large-scale load changes, the fixed-parameter MADRC fails to fully guarantee control performance.

Therefore, this paper proposed a gain-scheduling-based parameter adaptive MADRC strategy. Specifically, for the system models corresponding to different load conditions, inertial compensation modules are constructed, respectively, and the controller parameters are tuned and optimized by adopting appropriate parameter tuning methods. This improvement effectively enhances the tracking accuracy and anti-disturbance capability of the SST system under three typical operating conditions. The main contributions of this paper are summarized as follows:

(1) An adaptive modified active disturbance rejection control method is proposed for the superheated steam temperature system.
(2) A parameter tuning method is presented for the adaptive modified active disturbance rejection control.
(3) The effectiveness of the proposed method is verified through on-site applications. Notice that this method possesses the outstanding advantages of a simple principle, strong engineering practicability and high operational reliability and can significantly improve the control effect of the SST.

The paper is organized as follows: Section 2 introduces the structure and control model of the SST. Section 3 describes the control principle of ADRC and presents the proposed MADRC based on a parameter adaptation strategy. Section 4 compares the proposed MADRC with multiple controllers under different working conditions through simulations. Monte Carlo experiments are used to simulate scenarios with uncertain system parameters, verifying the control performance of the proposed method. The robustness and high-frequency noise suppression capability of the controller are also explored. The results demonstrate the effectiveness of the proposed control strategy. Section 5 applies the proposed method to a 660 MW unit for on-site application. Through the comparative analysis of the operation data before and after the method is put into use, the effectiveness of the proposed method is verified. Section 6 summarizes the paper and points out the broad application prospects of the proposed method.

2. Structure and Control Model of Superheated Steam Temperature System

The structure of the SST is shown in Figure 1. From Figure 1, it can be seen that the system is a two-stage process, which includes both low-temperature and high-temperature superheating stages. Steam exits the steam-water separator and enters the pipeline. It then goes through two superheating stages before entering the steam turbine. During this process, the temperature of the superheated steam is precisely controlled by adjusting the flow rate W of the attemperation water through the water injection valve. Throughout the

process, the output main steam temperature T is mainly influenced by the attemperation water flow W, the inlet steam flow D, and the flue gas heat Q. Among these, the attemperation water flow W is the control variable of the system, while the steam flow D and the flue gas heat Q are the main disturbance variables.

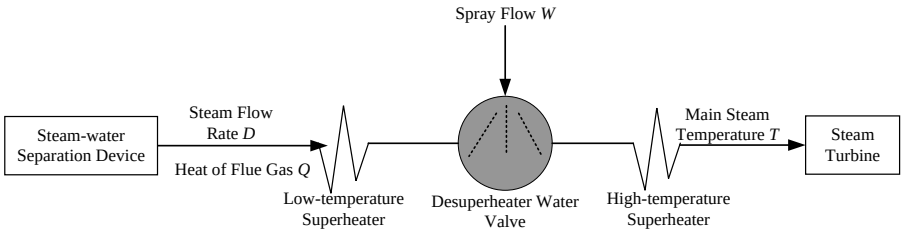


Figure 1. Schematic diagram of the superheated steam temperature system structure.

Ref. [36] takes the high-temperature superheater of a supercritical 600 MW once-through boiler as the study object. It analyzes the dynamic characteristics and uses a linearized distributed parameter method to build a model of the superheated steam temperature system at typical load points. This model has been widely adopted. The specific mechanism model is as follows [36]:

$$\frac{T_{exit}(s)}{D_{sp}(s)} = -K_{DT} \cdot e^{-\tau_0 s - \frac{\alpha_D T_m s}{1+T_m s} s} \tag{1}$$

where

$$\tau_0 = V \cdot \overline{\rho} / D \tag{2}$$

$$\alpha_D = (\alpha_2 \cdot A)/(D \cdot C_p) \tag{3}$$

$$T_m = (M \cdot C)/(\alpha_2 \cdot A) \tag{4}$$

$$\alpha_2 = B \cdot \frac{\lambda^{0.6} C_p^{0.4}}{\mu^{0.5}} \cdot D^{0.8} \tag{5}$$

$$K_{DT} = (I_1 - I_{sp})/(D \cdot C_{p1}) \tag{6}$$

In Equations (1)–(6), T_{exit} represents the outlet temperature of the superheater. D and D_{sp} are, respectively, the main steam flow rate and the water spray flow rate. C_p and C_{p1} are, respectively, the average specific heat at constant pressure of the working medium in the process and the specific heat at constant pressure of the working medium at the process outlet. I_1 and I_{sp} represent the enthalpy values of the steam at the water spray point and the enthalpy values of the desuperheating water, respectively; τ_0 is the average time for steam to flow through the heat-receiving tube; α_D is the dynamic parameter in the flow process; V and $\overline{\rho}$ are, respectively, the volume of the section and the average density of the steam within the section; T_m is the time constant for heat storage in metals; A and α_2 are, respectively, the internal surface area and convective heat release coefficient of the link; M and C are, respectively, the mass and specific heat of the metal in the wall tube; λ and μ are the thermal conductivity and dynamic viscosity of steam, respectively; B is a constant.

The model shown in Equation (1) can be regarded as a functional expression of the working condition parameters and can be represented by the high-order inertia link: $K/(Ts+1)^n$ [36]. Table 1 shows the transfer functions of the lead zone and inertia zone of the SST at three typical load points: 100%, 75%, and 50% load. It can be seen from Table 1 that the model parameters change significantly with load variation. Especially, the time constant of the inertia zone changes notably. Therefore, conventional controllers cannot meet the control performance requirements of the system under multiple load conditions. It is necessary to design a control strategy that ensures a good control effect across various load conditions.

Table 1. Multi-load SST system model.

Load/%	Leading Zone	Inert Zone
100	$-\frac{0.815}{(18s+1)^2}$	$\frac{1.276}{(18.4s+1)^6}$
75	$-\frac{1.657}{(20s+1)^2}$	$\frac{1.202}{(27.1s+1)^7}$
50	$-\frac{3.067}{(25s+1)^2}$	$\frac{1.119}{(42.1s+1)^7}$

3. The Design of Modified Active Disturbance Rejection Control

First-order and second-order ADRCs are the most widely used types of active disturbance rejection controllers in engineering practice. Based on the theory of the ESO, which treats complex dynamics and uncertainties in the system as "total disturbance", low-order ADRC can also control high-order systems. Moreover, it has been proven that low-order controllers can effectively control high-order systems in Ref. [37], and this approach has been applied in engineering practice. The following section discusses the first-order active disturbance rejection controller. Its structure is shown in Figure 2.

In general, the system can be described in the following form:

$$\dot{y} = \hat{f}(y, \ddot{y}, \tau, \cdots, d) + bu \tag{7}$$

where $\hat{f}$ is a composite function that includes unknown dynamic terms such as time delay constants (τ), high-order dynamics ($\ddot{y}$), and external disturbances (d). b is the uncertain input gain of the system. Equation (7) is modified to obtain the following equation:

$$\dot{y} = \hat{f} + bu + b_0 u - b_0 u = f + b_0 u \tag{8}$$

where $f = \hat{f} + (b - b_0)u$ is called the total disturbance (including both internal and external disturbances). b_0 is the estimated value of b and is a known quantity. By defining y as the extended state x_1, and defining f as the extended state x_2, the state-space representation of Equation (8) is expressed as:

$$\begin{cases} \begin{bmatrix} \dot{x}_1 \\ \dot{x}_2 \end{bmatrix} = \begin{bmatrix} 0 & 1 \\ 0 & 0 \end{bmatrix} \begin{bmatrix} x_1 \\ x_2 \end{bmatrix} + \begin{bmatrix} b_0 \\ 0 \end{bmatrix} u + \begin{bmatrix} 0 \\ 1 \end{bmatrix} \dot{f} \\ y = \begin{bmatrix} 1 & 0 \end{bmatrix} \begin{bmatrix} x_1 \\ x_2 \end{bmatrix} \end{cases} \tag{9}$$

For the first-order system shown in Equation (9), the corresponding second-order extended state observer can be expressed as

$$\begin{bmatrix} \dot{z}_1 \\ \dot{z}_2 \end{bmatrix} = \begin{bmatrix} -\beta_1 & 1 \\ -\beta_2 & 0 \end{bmatrix} \begin{bmatrix} z_1 \\ z_2 \end{bmatrix} + \begin{bmatrix} b_0 & \beta_1 \\ 0 & \beta_2 \end{bmatrix} \begin{bmatrix} u \\ y \end{bmatrix} \tag{10}$$

where β_1, β_2 are the gains of the observer. When β_1, β_2 are properly adjusted, z_2 can track the total disturbance f well.

The bandwidth parameterization method is used for tuning, as follows:

$$\begin{cases} \beta_1 = 2\omega_o \\ \beta_2 = \omega_o^2 \end{cases} \tag{11}$$

where ω_o is the observer bandwidth.

The state feedback control law is designed as

$$u = \frac{u_0 - z_2}{b_0} \tag{12}$$

Substituting Equation (12) into Equation (8) gives the compensated system as

$$\begin{aligned} \dot{y} &= f + b_0 u = f + b_0 \frac{u_0 - z_2}{b_0} \\ &\approx f + b_0 \frac{u_0 - f}{b_0} = u_0 \end{aligned} \tag{13}$$

where b_0 is the estimated value of b and can be manually assigned, and f is the total disturbance (including both internal and external disturbances). It can be seen that the system becomes an integral series structure. From Figure 2, the control law is given as

$$u_0 = k_p(r - z_1) \tag{14}$$

where r is the setpoint of the system, and k_p is the controller bandwidth. Both have clear physical meanings. The parameter d in Figure 2 represents an external disturbance.

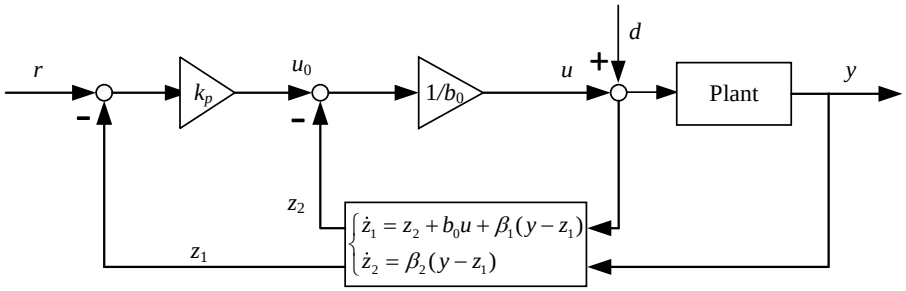


Figure 2. The structure of the first order ADRC.

Conventional ADRC has been applied in many fields. However, when used for systems with large inertia and high-order characteristics, its control performance is often not ideal. Due to the high-order inertia in the system, the ESO cannot accurately estimate the state and disturbance of high-order systems, resulting in limited control effectiveness. A modified active disturbance rejection control (MADRC) strategy is proposed by designing a compensation link to approximately eliminate the high-order inertial link in Refs. [35,38], thereby enhancing the state estimation accuracy of ESO and improving the control performance for objects with large inertia and high-order characteristics. The MADRC proposed is based on first-order ADRC. It adds a compensation module to approximately cancel the large inertia links in high-order systems. For the compensation module, its function is to delay the control signal before it enters the ESO. Due to the large inertia and large delay characteristics of the SST, the system output has already been delayed because of the high-order inertia characteristics of the system itself. When using a conventional ADRC controller, the problem of the output signal being out of sync with the control signal will occur. This module will make the control signal and output signal entering the ESO more synchronous, thereby approximately offsetting the high-order inertial characteristics of the controlled object and improving the control accuracy of the system. The SST can usually be described as $G_p(s) = K/(Ts + 1)^n$. The compensation module in the controller is selected as

$$G_{cp}(s) = \frac{1}{(Ts + 1)^{n-1}} \tag{15}$$

where T is the time constant of the compensation module. The design concept of MADRC is to compensate the controlled object into a system of order 1 through a compensation part before entering the ESO, as shown in Equation (16):

$$Y(s) = \frac{K}{(Ts+1)^n}U(s) = \frac{K}{(Ts+1)}\frac{1}{(Ts+1)^{n-1}}U(s) = \frac{K}{(Ts+1)}U_f(s) \tag{16}$$

where $U_f(s)$ is the output of the compensation part. Then, one of the input signals of ESO changes from the control signal u of the system to the output u_f of the compensation part. Equation (16) can be organized as

$$\dot{y} = \frac{K}{T}u_f - \frac{1}{T}y = b_0 u_f + \left(\frac{K}{T} - b_0\right)u_f - \frac{1}{T}y = b_0 u_f + f \tag{17}$$

where b_0 is the known input gain, and $f = (K/T - b_0)u_f - y/T$ is the total disturbance of the higher-order system after compensation. The structure of the MADRC can then be shown as in Figure 3.

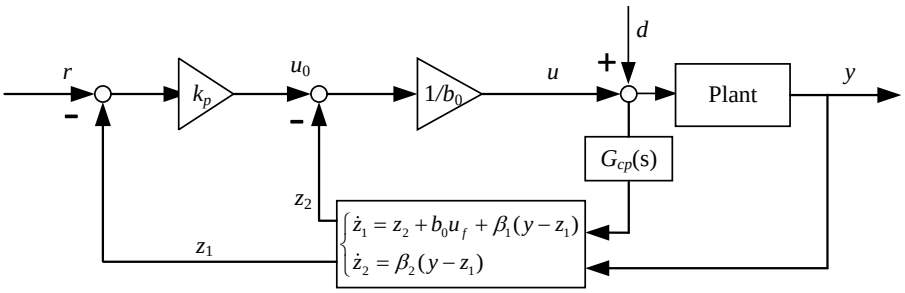


Figure 3. The structure of MADRC.

Thus, compared to the regular design of ADRC described above, the ESO of MADRC can be implemented as follows:

$$\begin{bmatrix}\dot{z}_1\\ \dot{z}_2\end{bmatrix} = \begin{bmatrix}-\beta_1 & 1\\ -\beta_2 & 0\end{bmatrix}\begin{bmatrix}z_1\\ z_2\end{bmatrix} + \begin{bmatrix}b_0 & \beta_1\\ 0 & \beta_2\end{bmatrix}\begin{bmatrix}u_f\\ y\end{bmatrix} \tag{18}$$

where u_f is the output of the compensation part, and the state feedback control law is the same as Equation (12).

By adding the compensation module, the control signal entering the ESO is delayed. This allows the system output and the delayed control signal to synchronize, enabling the ESO to estimate the system state with higher accuracy. Since the stability proof of MADRC has been elaborated in detail in Ref. [35], this article does not provide further explanations but instead focuses more on the design of MADRC.

Based on this, the parameters of the MADRC are tuned. As mentioned above, the parameters to be tuned for MADRC are ω_o, b_0, k_p, and T. Among these, T varies with the operating conditions and corresponds to three typical working points, so it does not require additional tuning. For the tuning of the three parameters ω_0, b_0, and k_p, the following rules can be referred to:

1. A larger k_p and a smaller b_0 both make the system respond quickly. However, too large k_p or too small b_0 can cause a large overshoot in the response and increase system fluctuations. When the value of b_0 falls within the interval $[K/2T, \infty)$, the ESO has good stability and convergence.
2. The disturbance compensation capability and observation ability increase with a larger ω_o. However, this also increases the noise in the ESO. Therefore, it is necessary to gradually increase the value of ω_o to an appropriate level to ensure the control

performance of the ESO. Based on extensive simulation experience, when the value of ω_o is in the range [0.3, 0.6], the system can maintain good control performance.

Based on the above tuning rules, a parameter tuning method for MADRC is developed through extensive simulation. The parameter tuning process is shown in Figure 4. The detailed steps are given below:

1. First, b_0 should be fixed, and its value should fall within $[K/2T, \infty)$.
2. Choose a small k_p and ω_o, then gradually increase the value of ω_o until the output shows no significant change. Record the value of ω_o at this point.
3. Gradually increase the value of k_p until the system achieves satisfactory control performance. Record the value of k_p at this point. If the control effect is not ideal, repeat the above steps until satisfactory performance is achieved.

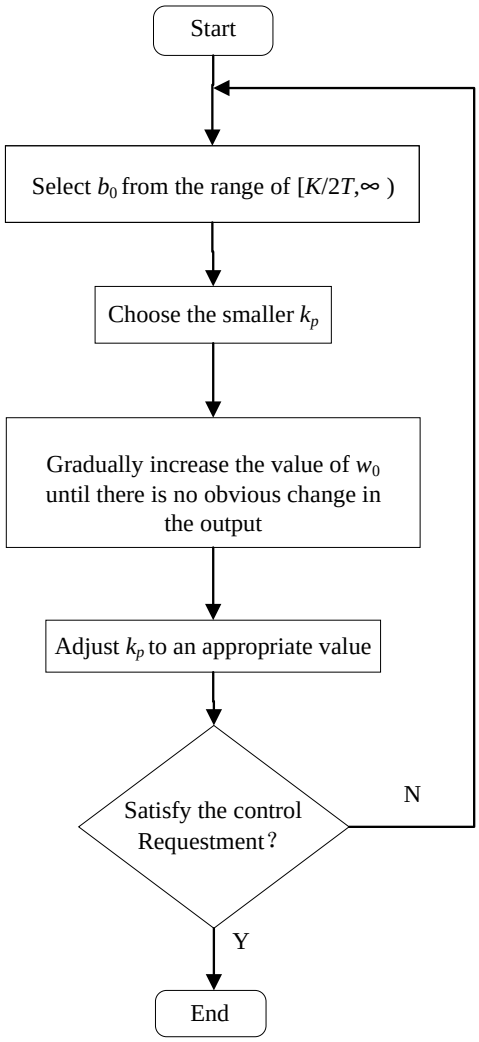


Figure 4. Flow chart of the MADRC tuning.

Based on the above discussion of how parameters affect control performance, how to select the adaptive parameter is discussed. Using the single-variable method to explore how different ω_o values influence the system output. As can be seen from the following Figure 5, when ω_o reaches a certain size, the control effect on the system basically remains unchanged. Therefore, it is only necessary to ensure that ω_o is within a reasonable range. As for b_0, since this parameter is the denominator in the control rate, a change in b_0 may cause a jump in the control rate. Therefore, in actual operation, b_0 is not selected as the adaptive parameter. Based on the above analysis, k_p is selected as the adaptive parameter for tuning.

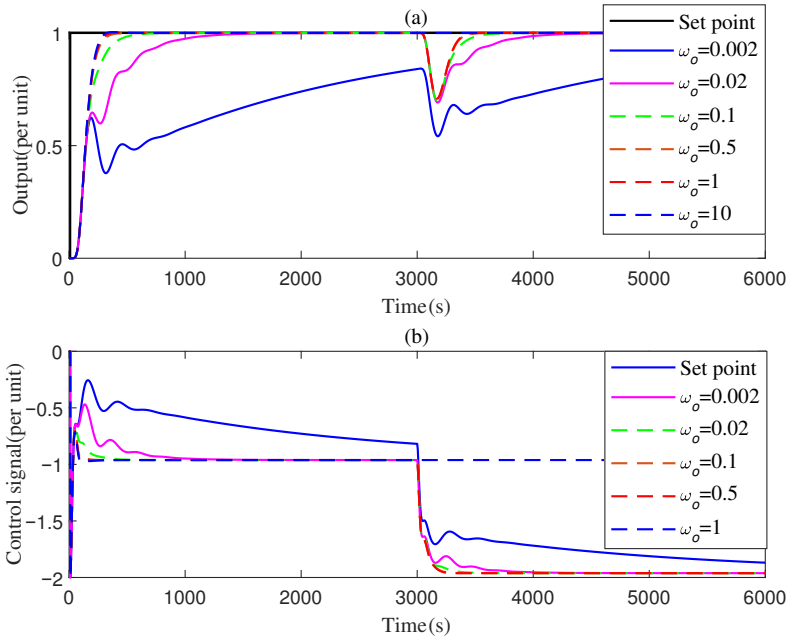


Figure 5. The influence of different ω_o on the control effect. ((**a**): the outputs; (**b**): the control signals).

To simplify the tuning process, b_0 is first fixed at 0.06, which meets the range requirement. Then, following the MADRC parameter tuning process shown in Figure 4, the tuned parameter $\omega_o = 0.3$ is obtained through extensive cyclic testing. The values of the adaptive gain coefficient k_p under 100%, 75%, and 50% load are 0.060, 0.055, and 0.050, respectively.

It should be noted that it has already been shown through simulation that the choice of model order has little effect on the model in Ref. [39]. Moreover, Figure 6 shows the open-loop step response of the inert region transfer function model and its approximate seventh-order model under 100% full load as described in this paper. It can be observed from the figure that the waveforms of the two are almost the same, and the approximate result essentially has little impact on the closed loop. Therefore, this paper approximates the inertia zone transfer function at 100% full load as a seventh-order system, which is: $G_p(s) = 1.276/(16.0s + 1)^7$. This ensures consistent system order across the three typical load conditions and facilitates the design of MADRC.

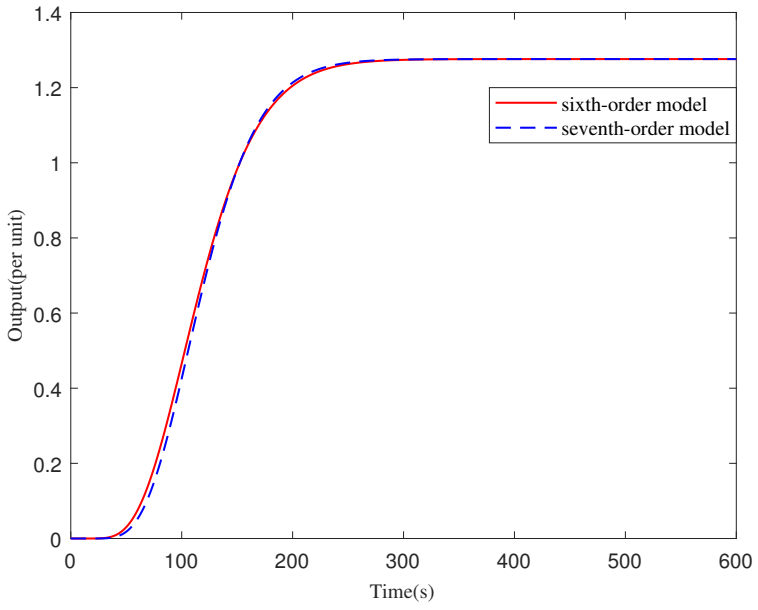


Figure 6. Open-loop step responses of sixth-order and seventh-order models.

4. Simulation Research

To verify the control effect of the proposed ADRC in the SST under variable load conditions, this experiment uses three controllers for comparison: the PID control based on integral gain adaptation from Ref. [40], the second-order ADRC based on the fruit fly algorithm from Ref. [41], and the nonlinear ADRC (NLADRC) from Ref. [12]. All the simulation experiments are conducted in the MATLAB 2023a version. In all control structures, the inner loop proportional control parameter is set to $k_{p1} = -2$. For the PID control based on integral gain adaptation, its parameters are $k_p = 0.6171$ and $k_d = 20.0000$. The values of the integral gain coefficient under 100%, 75%, and 50% load are $k_{i1} = 0.0075$, $k_{i2} = 0.0050$, and $k_{i3} = 0.0030$, respectively. For the outer loop second-order ADRC, its parameters are $k_p = 10^{-4}$, $k_d = 0.014$, $b_0 = 0.0073$, and $\omega_o = 1.33$. For the NLADRC, its parameters are $b_0 = 0.1$, $\beta_1 = 0.1$, $\beta_2 = 0.006$, $\beta_3 = 0.0003$, $\alpha_1 = 0.5$, $\delta_1 = 0.1$, $\alpha_2 = 1.0$, $\delta_2 = 0.001$.

Step tests of setpoint and input disturbance are applied to the above controllers under both nominal and uncertain conditions across multiple load levels. Their control performance is observed and compared.

4.1. Control Effect Under Nominal Working Conditions

Under nominal conditions, the setpoint is changed as a step signal at 10 s. A step disturbance is added to the outer loop at 2000 s, and to the inner loop at 4000 s. The system output and control signal under 100%, 75%, and 50% load conditions are shown in Figures 7–9.

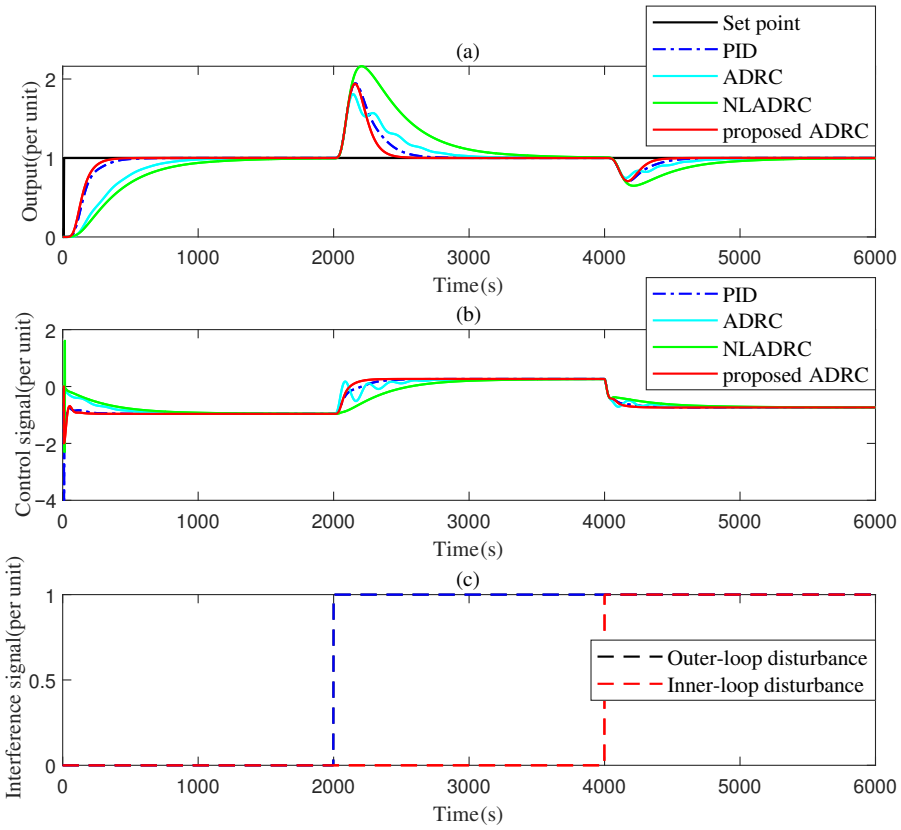


Figure 7. Control performance under 100% load. ((**a**): the outputs; (**b**): the control signals; (**c**): the interference signals).

From Figure 7, it can be observed that the proposed ADRC has the fastest tracking speed under 100% load. When the system is disturbed, it returns to the steady-state value in the shortest time. From Figure 8, it can be seen that under 75% load, the proposed

ADRC still responds and converges faster than PID, ADRC and NLADRC. From Figure 9, under 50% load, both ADRC and NLADRC show significant overshoot, and the response speed of NLADRC is very slow, while the PID control still has noticeable fluctuations after tracking convergence. The proposed ADRC produces no overshoot and almost no fluctuation during the simulation, demonstrating the best control performance.

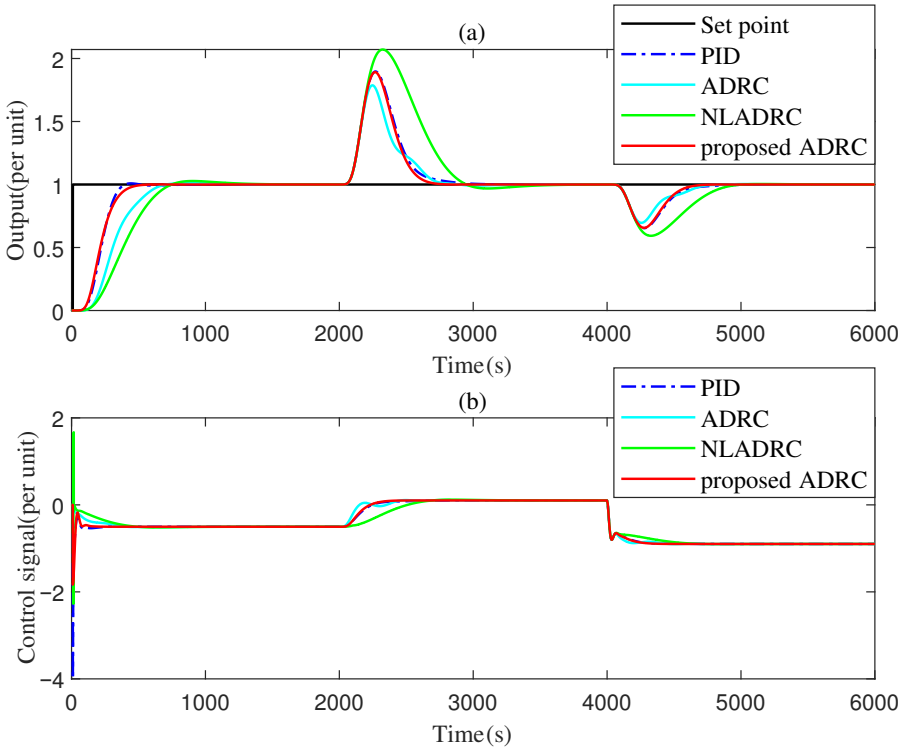


Figure 8. Control performance under 75% load. ((**a**): the outputs; (**b**): the control signals).

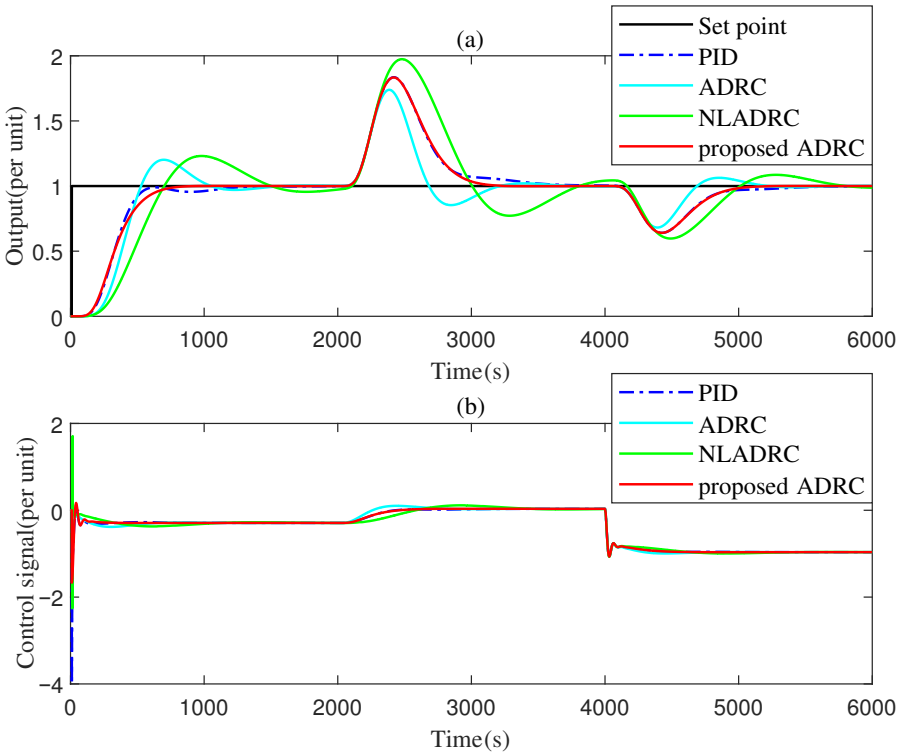


Figure 9. Control performance under 50% load. ((**a**): the outputs; (**b**): the control signals).

In addition, to test the control performance of the control strategy under different types of disturbances, a ramp disturbance with an amplitude of 2 and a change rate of 0.002, and a sine wave disturbance with an amplitude of 2 are selected for verification. The specific simulation process is as follows: At 10 s, the set value is stepped from 0 to 1. At 2000 s, an outer loop disturbance with a slope of 0.002 and an amplitude of 2 is added. At 5000 s, this disturbance is reduced to 0 at the same rate. At 10,500 s, a sinusoidal wave disturbance is given to the system. From Figure 10, it can be seen that the method proposed in this paper has the best anti-interference effect under different types of disturbances, thereby further verifying the effectiveness of the strategy proposed in this paper.

In summary, the proposed ADRC shows no overshoot at any of the three typical load points. When input disturbances occur, it tracks quickly without obvious fluctuations, showing high application potential.

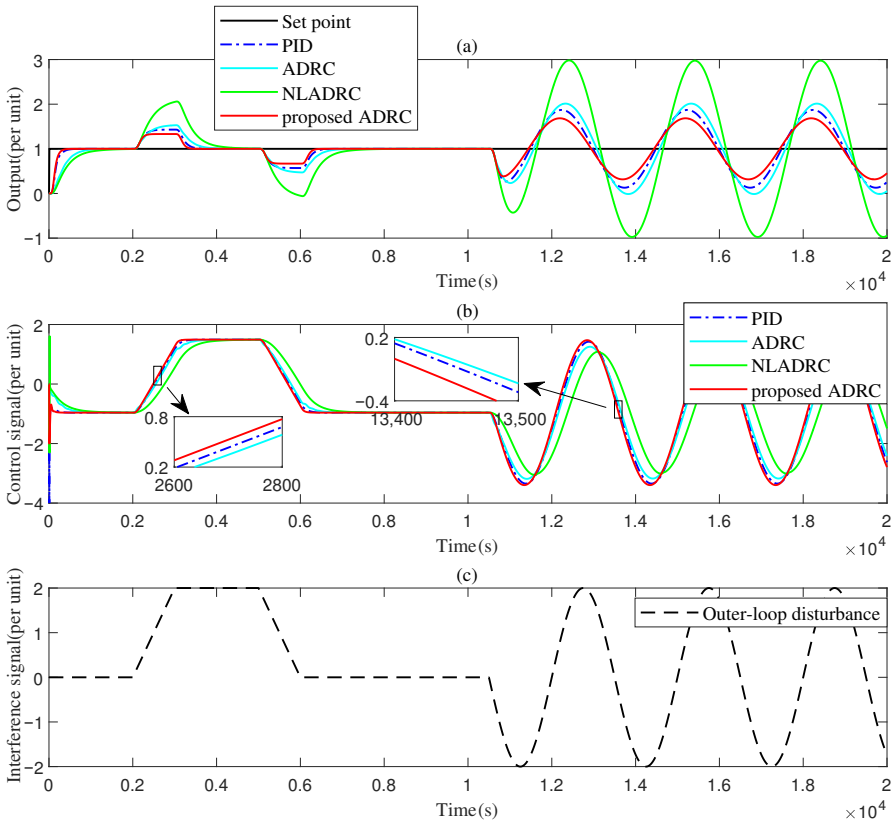


Figure 10. Control performance under different forms of disturbance. ((**a**): the outputs; (**b**): the control signals; (**c**): the interference signals).

4.2. Control Effect Under Uncertain Working Conditions

The SST is a typical nonlinear system with time-varying characteristics. It involves multi-physics coupling processes and has large time-delay elements, making it highly complex. Therefore, many simplifications are made during modeling, meaning the SST has strong uncertainty. It is necessary to examine whether the proposed control strategy can still achieve satisfactory performance under the above conditions. This paper uses Monte Carlo experiments to compare the control effects of various strategies when system uncertainty exists. The parameters of each controller are kept unchanged, while the time constants and gain coefficients in the transfer functions from Table 1 are randomly varied within ±10%. The simulation from Figures 7–9 is repeated 200 times, and the results are shown in Figures 11–13. As can be seen from Figure 11, the proposed ADRC achieves the best control performance at 100% load. The other three control strategies also keep the

output within an acceptable range under all three typical load points, indicating that all three strategies have strong robustness.

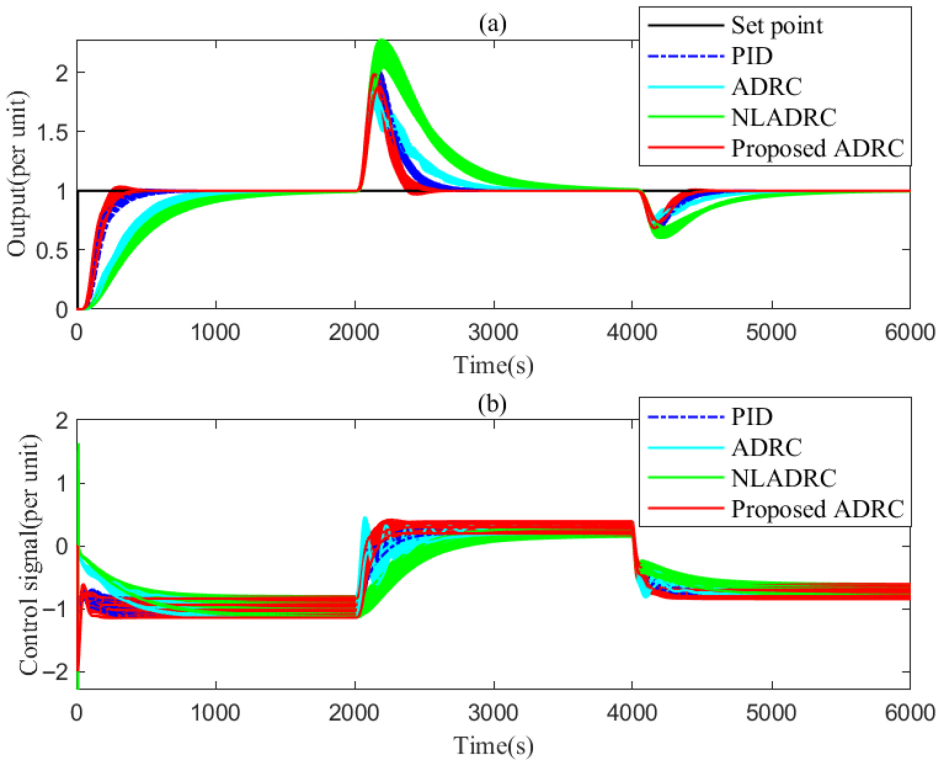


Figure 11. System robustness test under 100% load. ((**a**): the outputs; (**b**): the control signals).

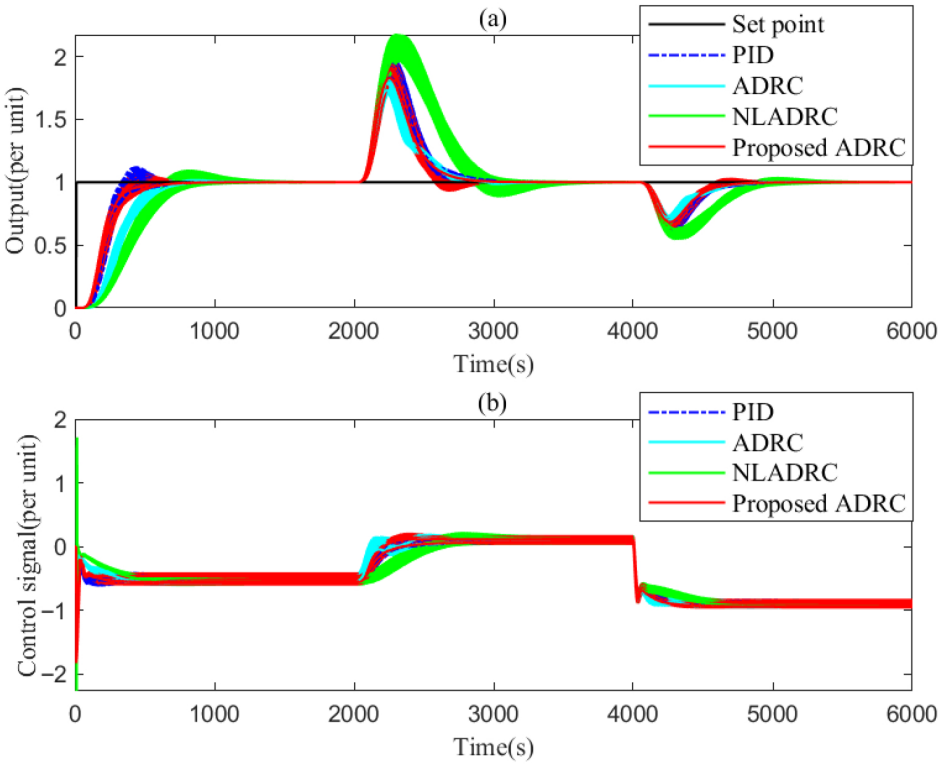


Figure 12. System robustness test under 75% load. ((**a**): the outputs; (**b**): the control signals).

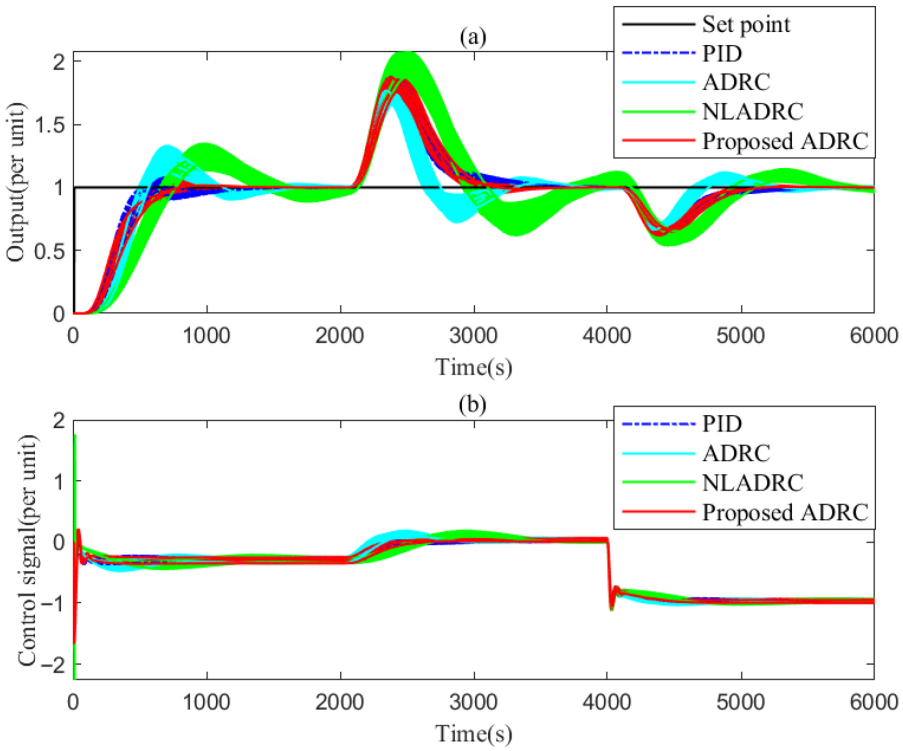


Figure 13. System robustness test under 50% load. ((**a**): the outputs; (**b**): the control signals).

4.3. Formatting of Mathematical Components

To better analyze the control capabilities of the three strategies quantitatively, the following performance metrics are calculated from the Monte Carlo experiments under the three typical load conditions: the integral absolute error (IAE), the overshoot, and the total variation (TV) of the control input. The formulas for IAE and TV are given below:

$$\mathrm{IAE} = \int_0^\infty |r(t) - y(t)| \mathrm{d}t \tag{19}$$

$$\mathrm{TV} = \sum_{i=0}^{n-1} |u(i+1) - u(i)| \tag{20}$$

It should be noted that a smaller IAE value indicates better control performance. This means the control strategy is more reliable under parameter changes and has stronger disturbance rejection ability. The TV index is defined as the sum of absolute differences in the control signal between adjacent time steps. A smaller TV value means the control signal is smoother and the actuator moves more gently. If the TV value is too large, it can cause mechanical wear on the actuator and harm stable system operation. From Figure 14, it can be observed that at 100% load, the proposed ADRC has the smallest IAE and TV values among the three control strategies. Although the proposed ADRC shows some large overshoot in a few simulations, the overall overshoot is kept within 1%, with a few cases within 4%, which is acceptable. From Figure 15, the proposed ADRC also has the smallest IAE value. Both its TV and overshoot are lower than those of PID and NLADRC, indicating that the proposed ADRC is more stable under parameter variations. From Figure 16, at 50% load, the IAE value of the proposed ADRC is similar to that of PID control, but its TV value is much smaller. The second-order ADRC shows overly scattered results and very high overshoot, which is no longer satisfactory. The NLADRC has the largest TV and IAE values, indicating that its performance is the worst among the three controllers. In summary, the proposed ADRC provides the strongest control performance against system

uncertainty across the 50% to 100% load range. It also shows high robustness and great application value.

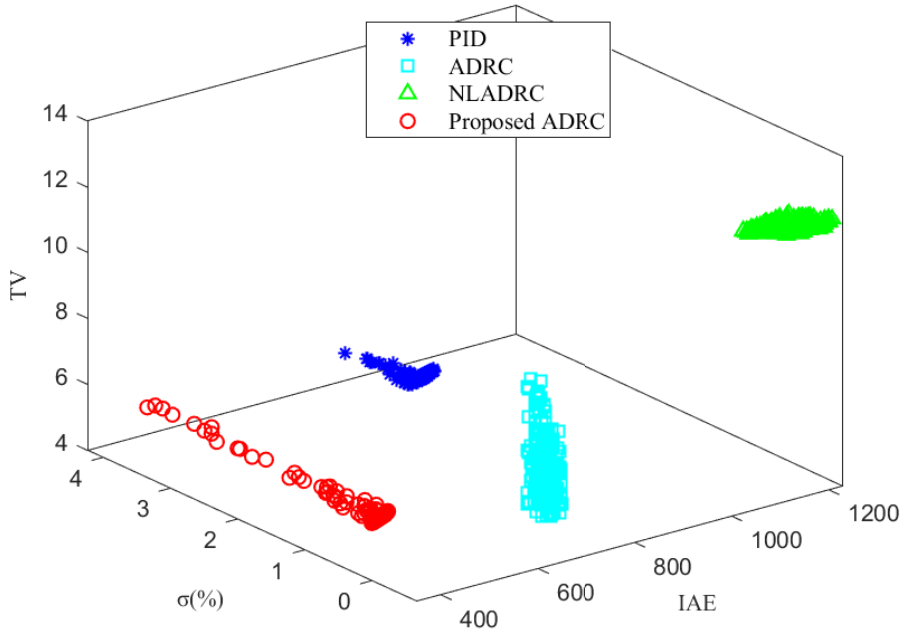


Figure 14. Indicator distributions under 100% load.

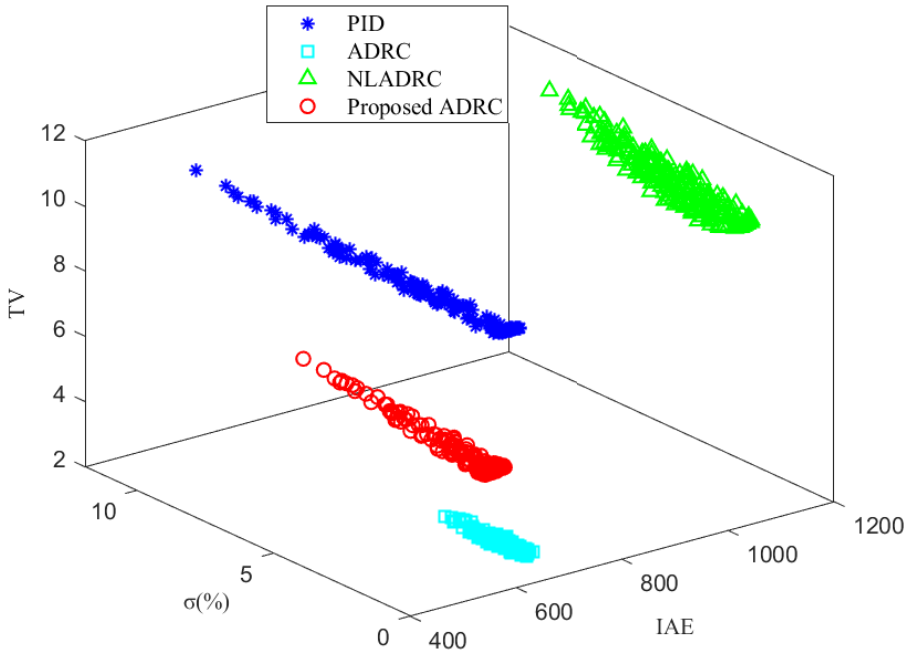


Figure 15. Indicator distributions under 75% load.

To conduct a more in-depth robustness analysis, M_s constraints are adopted to measure the robustness of the controller. Since M_s represents the frequency-domain index of a linear system, and NLADRC is essentially a nonlinear controller, it is impossible to analyze its M_s index. Therefore, we only conducted analyses on PID, ADRC and MADRC. The maximum sensitivity function is often selected as the robustness index, and it is defined as

$$M_s = \max_{\omega} |S(i\omega)| = \max_{\omega} \left| \frac{1}{1 + G_c(i\omega)G_p(i\omega)} \right| \tag{21}$$

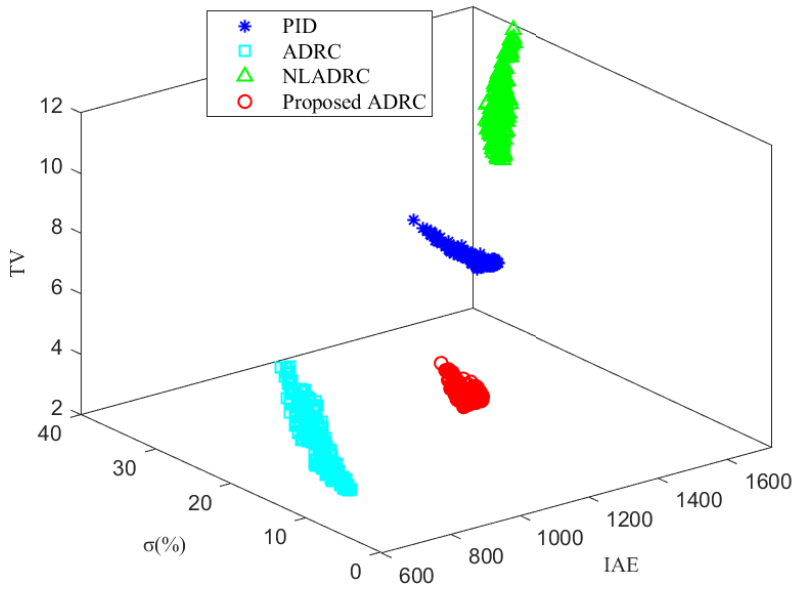


Figure 16. Indicator distributions under 50% load.

The M_s constraint can be described as the reciprocal of the shortest distance from a point to $(-1, 0j)$ on the Nyquist curve of an open-loop system. The smaller the M_s, the better the robustness of the controller. The reasonable range of M_s is 1.2 to 2.0. Figure 17 shows the Nyquist plots of three controllers under 100% load. It can be observed that the frequency characteristic trajectory of PID is the farthest from the center of the circle, that of ADRC is the closest, and MADRC is between the two and closer to PID. This indicates that both PID and MADRC have good robustness, while ADRC has poor robustness. Although the robustness of PID is better than that of MADRC, the robustness of MDADRC under 100% load is acceptable. Table 2 presents the M_s values of each controller under three typical operating conditions. As can be seen from Table 2, the M_s value of MADRC under 75% load conditions is not much different from that of PID, while it outperforms PID under 50% load industrial control conditions. Overall, MADRC has excellent robustness and can perform well even when the system is operating at low load. Compared with other controllers, it has better robustness.

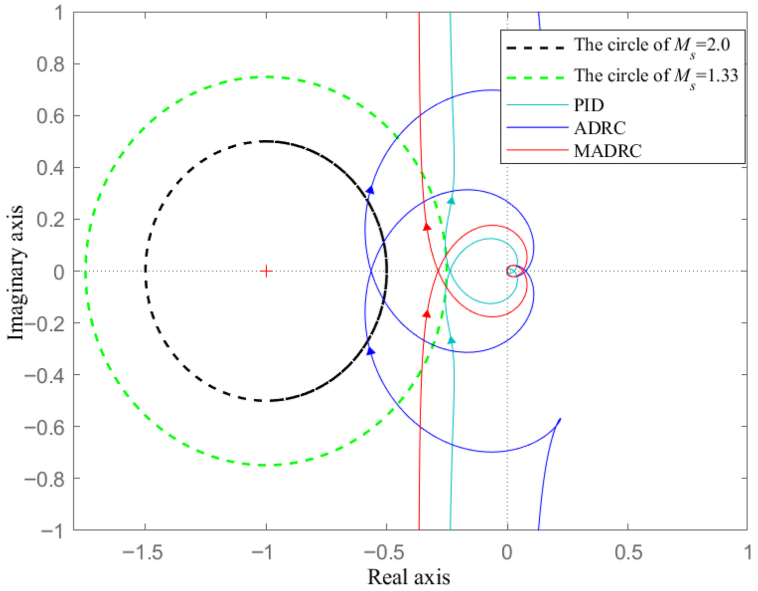


Figure 17. The Nyquist diagram with different controllers under 100% load. ((+) represents the point (−1, 0j), and the arrow indicates the direction of increasing frequency).

Table 2. The M_s values of different controllers under three typical operating conditions.

	100% Load	**75% Load**	**50% Load**
PID	1.3359	1.4856	1.5490
ADRC	2.3473	1.8381	1.7820
MADRC	1.4585	1.4928	1.4550

In addition, it is equally important to analyze the controller's sensitivity to noise. Take MADRC as an example to analyze the derivation process of high-frequency noise. MADRC can be transformed into the TDOF equivalent form as shown in Figure 18 through Mason's gain formula.

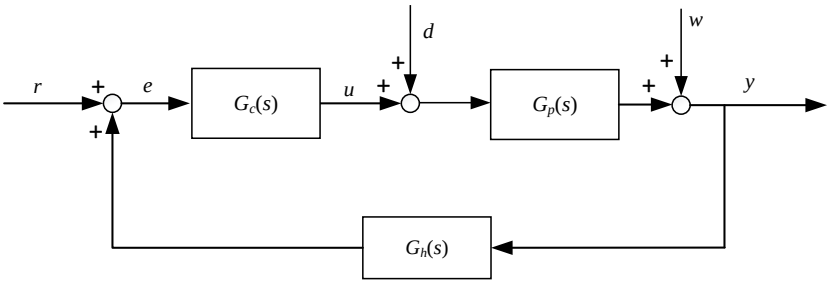


Figure 18. The TDOF equivalent form of MADRC.

In Figure 18, d represents the external disturbance and w represents the external noise. Then, the high-frequency noise suppression capability of MADRC can be described by the transfer function from w to u,

$$G_{wu_M} = \frac{-G_c(s)G_h(s)}{1 + G_c(s)G_h(s)G_p(s)} \tag{22}$$

where

$$G_c(s) = \frac{\frac{k_p}{b_0}(s^2 + \beta_1 s + \beta_2)}{s^2 + \beta_1 s + k_p G_{cp}(s)s + \beta_2[1 - G_{cp}(s)]} \tag{23}$$

$$G_h(s) = \frac{k_p(\beta_1 s + \beta_2) + \beta_2 s}{k_p(s^2 + \beta_1 s + \beta_2)} \tag{24}$$

$$G_p(s) = \frac{-2k_1k_2[(T_1s + 1)^{n_1} - 2k_1]}{(T_1s + 1)^{2n_1}(T_2s + 1)^{n_2}} \tag{25}$$

Among them, k_1, T_1, and n_1 are parameters in the leading zone model, while k_2, T_2, and n_2 are parameters in the inert zone model. According to Equations (22)–(25) [25], we can obtain

$$G_{wu_M} \underset{s\to\infty}{\sim} -\frac{k_p\beta_1 + \beta_2}{b_0}\frac{1}{s} = \Lambda_{wu_M}\frac{1}{s} \tag{26}$$

The larger the value of Λ_{wu_M} is, the stronger the system's ability to suppress high-frequency noise will be; conversely, the smaller the value is, the weaker the ability will be. Similarly, ADRC and PID can also be described in this way,

$$G_{wu_A} \underset{s\to\infty}{\sim} -\frac{\beta_3 + k_d\beta_2 + \beta_1 k_p}{b_0}\frac{1}{s} = \Lambda_{wu_A}\frac{1}{s} \tag{27}$$

$$G_{wu_PID} \underset{s\to\infty}{\sim} -k_d s^2\frac{1}{s} = \Lambda_{wu_PID}\frac{1}{s} \tag{28}$$

Table 3 shows the values of Λ_{wu} for the three controllers under the three working conditions. From the data in Table 1, it can be seen that the values of MADRC are much

larger than those of ADRC and PID under all three working conditions, indicating that MADRC has the best ability to suppress high-frequency noise.

Table 3. The Λ_{wu} values of different controllers under three typical operating conditions.

	100% Load	**75% Load**	**50% Load**
MADRC	−2.10	−2.05	−2.00
ADRC	−332.51	−332.51	−332.51
PID	−∞	−∞	−∞

To observe more intuitively the noise suppression capabilities of the three controllers, a noise with a power of 0.0005 is applied to the system. Figures 19–21 show the control effects of each controller after adding noise under three typical loads. It can be seen from the output curves in Figures 19–21 that the three controllers all have good high-frequency noise suppression capabilities under the three typical working conditions, and the output fluctuations are all within an acceptable range. By observing the control signal curve, it can be seen that the signal fluctuations of PID control and ADRC are both very strong and large in amplitude, indicating that PID and ADRC have undergone frequent and large-scale adjustments to counteract the noise. In contrast, the control signal of MADRC fluctuates the least, indicating the mildest adjustment. The greater the fluctuation amplitude of the control signal, the more frequently the actuator operates, and the higher the wear. To sum up, all three controllers have good high-frequency noise suppression capabilities. Among them, MADRC has the most stable control signal, the least actuator burden and the best performance.

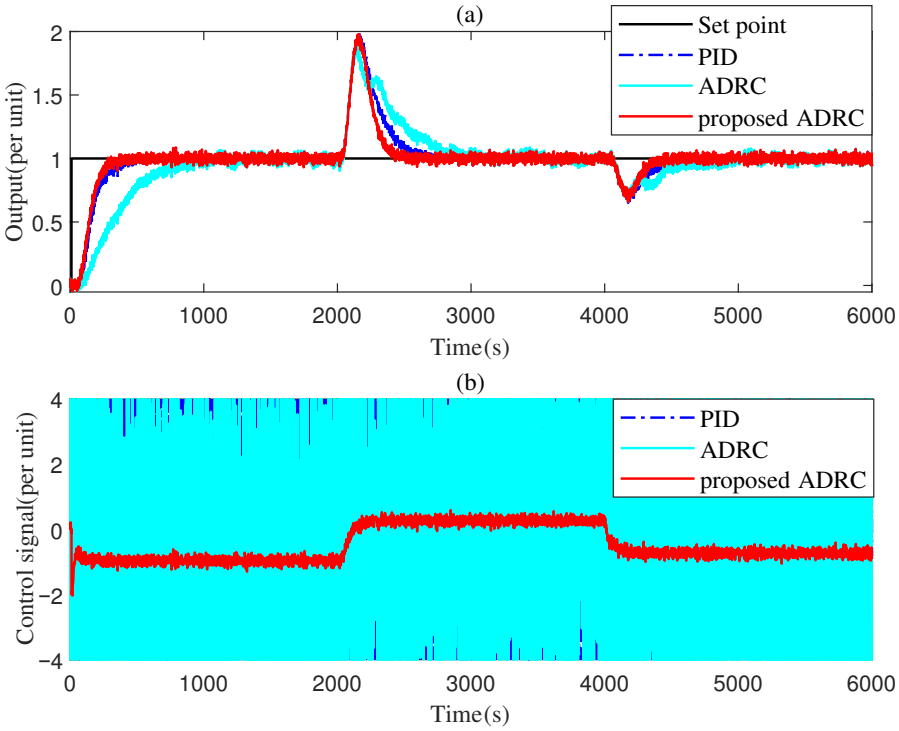


Figure 19. The control effect of each controller under 100% load. ((**a**): the outputs; (**b**): the control signals).

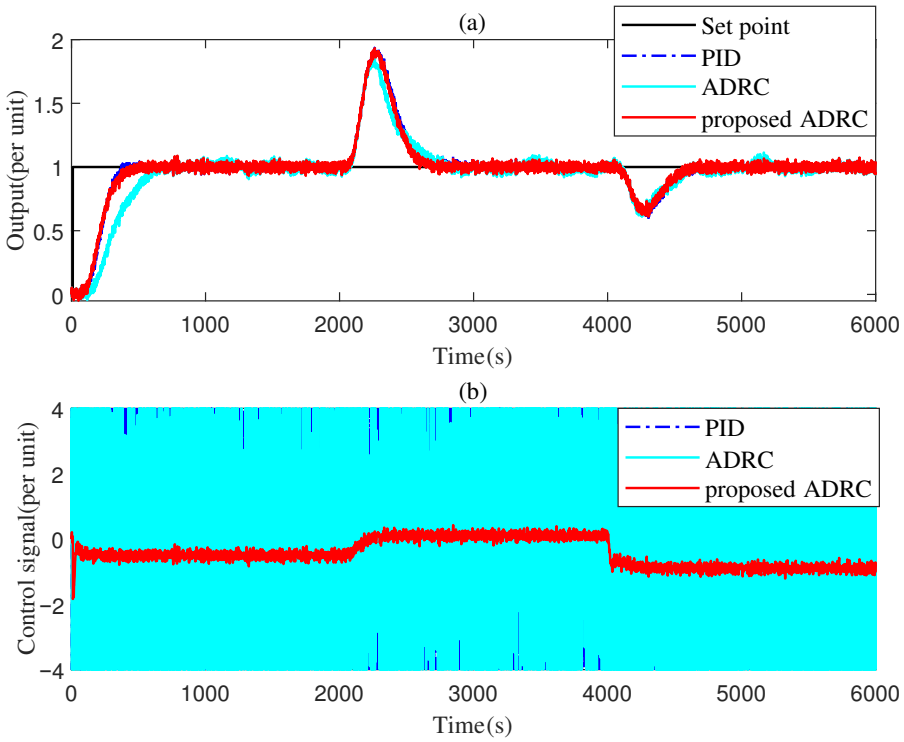


Figure 20. The control effect of each controller under 75% load. ((**a**): the outputs; (**b**): the control signals).

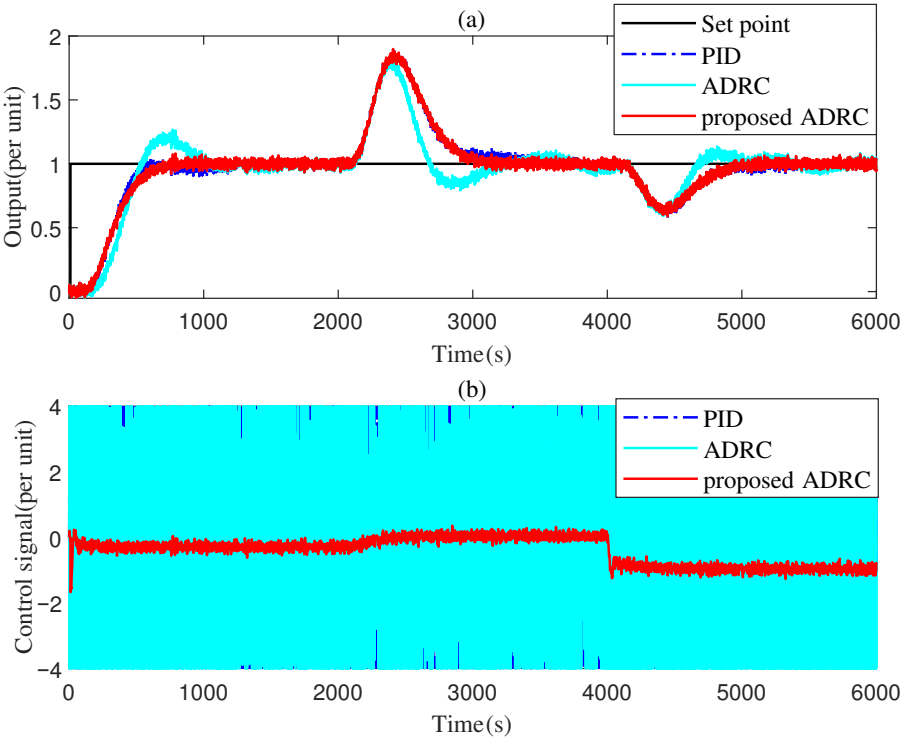


Figure 21. The control effect of each controller under 50% load. ((**a**): the outputs; (**b**): the control signals).

In total, the proposed MADRC is based on the idea of synchronizing the system output y and the control input u. However, it has many improvements compared to the conventional ADRC. The main features are summarized as follows:

(1) The proposed MADRC does not add any additional tuning parameters compared to the standard ADRC, and the method of parameter tuning is simple.

(2) The proposed MADRC inherits the simple structure feature of the standard ADRC, making it easy to be implemented in the DCS system without additional cost investment.
(3) While ensuring robustness, the proposed MADRC can improve the tracking performance and anti-interference ability of the system.
(4) The proposed MADRC can enhance the estimation ability of ESO through synchronizing y and u, and also increases the upper limit of the observer bandwidth of ESO.
(5) The proposed MADRC is applicable to a wide range of load conditions and various working scenarios, not limited to a specific working point.

In addition, Table 4 summarizes the comparison of the core characteristics of various modified ADRC controllers, including ADRC, time-delay ADRC, Smith-predictive ADRC, MADRC, and the MADRC proposed in this paper. From Table 4, the similarity among several modified ADRCs lies in that they are all based on the structure of conventional ADRC and incorporate different modules to enhance the control performance of systems with large inertia characteristics and time delays. The difference lies in the different methods adopted and the different effects achieved. Compared with time-delay ADRC, Smith-predictive ADRC and MADRC, the adaptive MADRC proposed can not only synchronize ESO input signals without causing output oscillations, but also improve the control performance of the system under wide loads and variable operating conditions, and has a very good application prospect.

Table 4. Comparison of core characteristics among different ADRC variants.

Controller Type	Core Architecture	Design Goal	Added Module
ADRC	ESO + disturbance compensation, simplify system to $\dot{y} \approx u_0$	Handle system uncertainty and external disturbance	No extra module
Time-delay ADRC	Inherit conventional ADRC architecture	Solve ESO signal asynchrony caused by output delay	Pure time-delay module
Smith-predictive ADRC	Inherit conventional ADRC architecture	Solve ESO signal asynchrony caused by output delay	Output prediction module
MADRC	Inherit conventional ADRC architecture	Solve ESO signal asynchrony caused by output delay	Inertia link compensation
Adaptive MADRC	Based on MADRC, add a parameter adaptive method	Improve performance under wide load conditions, solve oscillation of time-delay ADRC	Parameter adaptive method

5. Field Application

To further test the effectiveness of the method proposed in this paper, open-loop identification is used to build system models of a 660 MW supercritical unit under 100%, 75%, and 50% load. Following the approach presented, the parameters for the adaptive modified ADRC are obtained using the method shown in Figure 4. The modified ADRC is then implemented in the unit's distributed control system through logic configuration. A linear parameter switching rate is designed.

$$k_p = \begin{cases} k_{p1}, & P = 100\%\text{Pe}; \\ \frac{k_{p1}-k_{p2}}{175}(660 - P) + k_{p1}, & 75\%\text{Pe} < P < 100\%\text{Pe}; \\ k_{p2}, & P = 75\%\text{Pe}; \\ \frac{k_{p2}-k_{p3}}{175}(495 - P) + k_{p2}, & 50\%\text{Pe} < P < 75\%\text{Pe}; \\ k_{p3}, & P = 50\%\text{Pe}; \end{cases} \quad (29)$$

and

$$T = \begin{cases} T_1, & P = 100\%\text{Pe}; \\ \frac{T_1 - T_2}{175}(660 - P) + T_1, & 75\%\text{Pe} < P < 100\%\text{Pe}; \\ T_2, & P = 75\%\text{Pe}; \\ \frac{T_2 - T_3}{175}(495 - P) + T_2, & 50\%\text{Pe} < P < 75\%\text{Pe}; \\ T_3, & P = 50\%\text{Pe}; \end{cases} \tag{30}$$

Here, P represents the unit load, and Pe is the rated load of the unit. In addition, some on-site details need to be explained. The sampling period of the DCS system used on-site is 250 ms, and it adopts K-type thermocouple sensors with a resolution of 0.1. Regarding the actuator restrictions, the controlled quantity is the valve opening degree, and its constraint is 0–100. For communication latency, on-site transmission is all carried out through hardwiring, so its communication latency is relatively small and can basically be ignored compared to the thermal inertia in the system. A comparison of performance before and after applying the proposed method is shown in Figure 22. The unit load varies between 50% and 100%. After the method is applied, the fluctuation in SST becomes significantly smaller. Table 5 shows the statistics of the maximum and minimum values of the superheated steam temperature before and after the introduction of the method proposed in this paper. After calculation, the fluctuation range on sides A and B is reduced to only 34.0% and 53.0% of the original, respectively. The variance of the fluctuation on sides A and B is only 28.5% and 43.3% of the original, respectively. In summary, these results fully demonstrate the effectiveness of the proposed method.

It should be noted that for the set value strategy, the first thing to clarify is that the higher the set value, the better. However, if the superheated steam temperature is too high, it will cause irreversible damage to the superheated steam temperature pipeline, affecting the safety of the unit. If the temperature is too low, it will reduce the economic efficiency of the unit. In practical applications, as shown in Figure 22, there is a situation where the set value changes before the proposed method is put into use. This is because during actual operation, the temperature of the superheated steam needs to be constantly monitored. If it is too high, it will be lowered; if it is too low, it will be raised. This means that more intervention is required during operation, the burden is greater, and the control effect is not good. After the proposed method is put into use, the set value can remain unchanged for a period of time. This indirectly verifies the effectiveness of the proposed method.

It should also be noted that the actuator is a desuperheating water valve opening degree, with a constraint range of 0 to 100. Taking Figure 22 as an example, it drops to the lower limit of 0 at 500 s and is opened to the upper limit of 100 around 2300 s to adjust the temperature of the superheated steam.

Remark: For the division of working conditions, it is carried out according to the working conditions of 100%, 75% and 50% load in Equation (29). The more working condition divisions there are, the higher the precision of control will be, but at the same time, it will also increase the workload of parameter design and the implementation difficulty in the DCS system. To achieve a balance between higher precision and workload, the above division is chosen to avoid excessive complexity while ensuring accuracy.

Table 5. The values of the superheated steam temperature on sides A and B before and after investment.

	Before Investment (°C)			**After Investment (°C)**		
	Max	**Min**	**Difference**	**Max**	**Min**	**Difference**
A-side	605.731	586.417	19.314	601.948	585.384	6.564
B-side	607.599	580.739	26.860	601.635	588.525	13.110

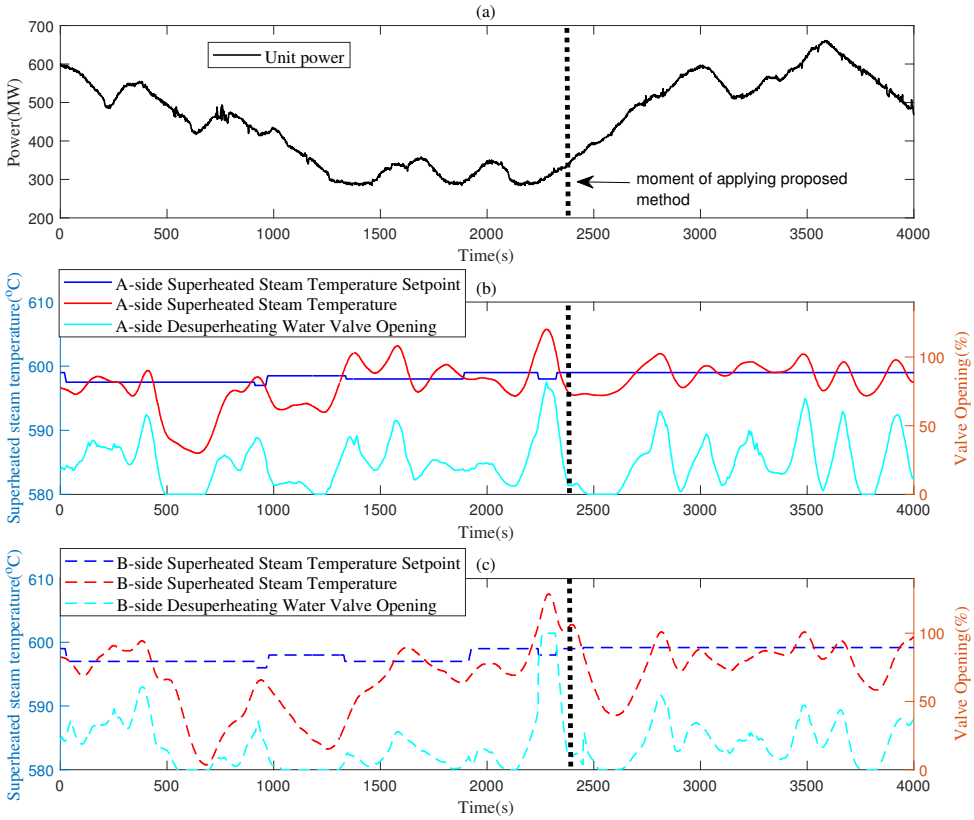


Figure 22. Operation data of a 660 MW unit. ((**a**): the unit load; (**b**): A-side superheated steam temperature; (**c**): B-side superheated steam temperature).

6. Conclusions

This paper introduces a modified active disturbance rejection control strategy based on parameter adaptation. It aims to solve the control problems caused by high-order inertial parts in SST. The study first describes the SST and its models at three common load points: 100%, 75%, and 50% load. The basic control idea of active disturbance rejection control (ADRC) is also explained. A modified ADRC strategy with parameter adaptation is proposed. This strategy uses a cascade control structure. In this setup, the inner loop uses a PI controller, and the outer loop uses the modified ADRC controller. A method for setting the parameters of the modified ADRC is given. Parameter adjustment is also performed for system models under different load conditions. The control effect of the proposed method is tested by simulation. The tests include both normal and uncertain working conditions. Moreover, real operation data from a 660 MW unit show that the proposed control strategy works well. The fluctuation range on sides A and B is reduced to only 34.0% and 53.0% of the original, respectively. The variance of the fluctuation on sides A and B is only 28.5% and 43.3% of the original, respectively. The above field application results fully demonstrate that the control strategy proposed does not merely remain at the theoretical simulation level but is a key technical means that can be effectively implemented and effectively solve the problem of superheated steam temperature control in thermal power units. This strategy, through precise disturbance compensation and parameter adaptation, significantly reduces the amplitude and dispersion of steam temperature fluctuations, greatly enhancing the stability and safety of the unit operation, and providing a practical and feasible engineering solution for high-precision SST control. In future work, we will focus on the quantitative research of parameters and further delve into the study of working condition division intervals to enhance control effectiveness without increasing complexity. In addition, we will further derive the mathematical relationship between the load percentage and the

controller bandwidth in subsequent research so as to better prove the system's adaptability. Meanwhile, in the subsequent research, we will also explore the scheme of integrating MADRC with fault diagnosis technology in order to further enhance the overall reliability of the system.

Author Contributions: Conceptualization, H.W. and Z.W.; investigation and writing—original draft, H.W.; methodology, H.W., Z.T. and Z.W.; validation, H.Z., B.L. and Y.J.; formal analysis, H.Z., B.L. and Y.J.; data curation, Z.T. and H.Z.; resources, H.W. and Z.W.; project administration, supervision and writing—review and editing, Z.W. All authors have read and agreed to the published version of the manuscript.

Funding: This work was supported in part by the Natural Science Foundation of Henan Province under Grant No. 252300421954, the Zhengzhou University Professor Team for the Enterprise Innovation-Driven Development Project under Grant No. JSZLQY2022016, and the Zhongyuan Scientific and Technological Innovation Leading Talent of Henan Province under Grant No. 254000510010.

Data Availability Statement: The original contributions presented in this study are included in the article. Further inquiries can be directed to the corresponding author.

Conflicts of Interest: Author Zhenlong Wu was employed by the Huadian Zhengzhou Mechanical Design Institute Company Limited. Author Bing Li was employed by the Rundian Energy Science and Technology Company Ltd. Yanfeng Jia was employed by the Sanmenxia Power Supply Company, State Grid Henan Electric Power Company. The remaining authors declare that the research was conducted in the absence of any commercial or financial relationships that could be construed as potential conflicts of interest.

Abbreviations

The following nomenclatures and abbreviations are used in this manuscript:

SST	Superheated Steam Temperature
PID	Proportional–Integral–Derivative
ADRC	Active Disturbance Rejection Control
ESO	Extended State Observer
TD	Time-Delayed
FOPTD	First-Order Plus Time-Delay
DIC	Delay-Inertia-Compensation
SOPTD	Second-Order Plus Time-Delay
WECS	Wind Energy Conversion Systems
PMSG	Permanent Magnet Synchronous Generators
P&O	Perturb and Observe
DC-DC	Direct Current to Direct Current
MPPT	Maximum Power Point Tracking
PMSM	Permanent Magnet Synchronous Motor
MADRC	Modified Active Disturbance Rejection Control
IAE	Integral Absolute Error
TV	Total Variation
NLADRC	Nonlinear ADRC
TDOF	Two-Degree-of-Freedom
DCS	Distributed Control System

References

1. Yao, Y.; Lu, Z.N.; Gong, Y.L.; Guo, S.; Xiao, C.P.; Hu, W.B. Drying characteristics of a combined drying system of low-pressure superheated steam and heat pump. *Processes* **2022**, *10*, 1402. [CrossRef]
2. Jiang, C.; Qian, H.; Pan, Y.K.; Chai, T.T. The research of superheated steam temperature control based on generalized predictive control algorithm and adaptive forgetting factor. *Int. J. Adapt. Control Signal Process.* **2020**, *34*, 15–31. [CrossRef]

3. He, T.; Wu, Z.L.; Li, D.H.; Wang, J.H. A tuning method of active disturbance rejection control for a class of high-order processes. *IEEE Trans. Ind. Electron.* **2020**, *67*, 3191–3201. [CrossRef]
4. Liang, W.Z.; Cui, Z.P.; Ma, S.X.; Xu, J. Optimization control of superheated steam temperature of supercritical boiler based on the prediction of the enthalpy at intermediate point. *J. Eng. Therm. Energy Power* **2025**, *40*, 73–82. [CrossRef]
5. Wu, H.G.; Shi, J.K.; Xu, S.D.; Gao, Z.Y. Feed forward control and on-line correction method for superheated steam temperature of thermal power units. *J. Eng. Therm. Energy Power* **2022**, *37*, 177–182. [CrossRef]
6. Luo, Y.; Wang, W. Superheated steam temperature sliding mode control based on modified super-twisting algorithm. *J. Chin. Soc. Power Eng.* **2020**, *40*, 475–480. [CrossRef]
7. Fan, H.; Su, Z.G.; Peng, X.Y.; Zhou, H.C. Anti-disturbance coordinated control system of once-through boiler coal fired units coupled with superheated steam temperature regulation. *Proc. CSEE* **2025**, *45*, 1010–1022. [CrossRef]
8. Cao, Y.; Zheng, L.; Chen, Y.F.; Wang, P.; Si, F.Q. Identification method and control strategy for superheated steam temperature of thermal power unit based on PFNN. *J. Southeast Univ. Sci. Ed.* **2022**, *52*, 417–424. [CrossRef]
9. Ma, L.Y.; Yu, S.L.; Zhao, S.Y.; Sun, J.M. Superheated steam temperature prediction models based on XGBoost optimized with random search algorithm. *J. North China Electr. Power Univ.* **2021**, *48*, 99–105. [CrossRef]
10. Feng, L.H.; Nie, C.P.; Guo, Q.F.; Yang, F.; He, J.Q.; Mao, Y.C. Superheated steam temperature prediction based on long short-term memory neural network optimized by novel whale optimization algorithm. *Power Gener. Technol.* **2025**, *46*, 1212–1222. [CrossRef]
11. Ma, L.Y.; Chen, T.T.; Liu, W.J.; Li, Q.Q. Optimized compensation for set values of superheated steam temperature in supercritical unit based on neural network. *J. Chin. Soc. Power Eng.* **2021**, *41*, 36–42. [CrossRef]
12. Han, J.Q. From PID to active disturbance rejection control. *IEEE Trans. Ind. Electron.* **2009**, *56*, 900–906. [CrossRef]
13. Li, D.L.; An, Z.G.; Zhou, Y.F.; Zhang, J.P.; Gao, Z.Y. Optimal control of cooling performance using an active disturbance rejection controller for lithium-ion battery packs. *Energy* **2025**, *322*, 135556. [CrossRef]
14. Pang, D.W.; Niu, Y.G.; Du, M. Phase lead error-based active disturbance rejection control for 1000 MW ultra-supercritical unit under flexible operation. *Energy* **2025**, *319*, 134946. [CrossRef]
15. Xu, H.B.; Zhang, J.D.; Liu, J.L.; Cao, Y.; Ma, A. Optimization of ship permanent magnet synchronous motor ADRC based on improved QPSO. *Appl. Sci.* **2025**, *15*, 1608. [CrossRef]
16. Sun, L.; Xue, W.C.; Li, D.H.; Zhu, H.X.; Su, Z.G. Quantitative tuning of active disturbance rejection controller for FOPTD model with application to power plant control. *IEEE Trans. Ind. Electron.* **2022**, *69*, 805–815. [CrossRef]
17. Wu, Z.L.; Jia, B.K.; Li, B.N.; Liu, Y.H.; Chen, Y.Q. Delay-inertia-compensation active disturbance rejection control design and analyses for second-order plus time-delay systems. *IEEE Trans. Ind. Electron.* **2025**, *72*, 14603–14614. [CrossRef]
18. Li, Z.; Zhang, Z.H.; Wang, J.S.; Wang, S.H.; Chen, X.T.; Sun, H.X. ADRC control system of PMLSM based on novel non-singular terminal sliding mode observer. *Energies* **2022**, *15*, 3720. [CrossRef]
19. Wu, Z.L.; Sui, S.Y.; Li, S.Y.; Li, B.N.; Liu, Y.H.; Yang, L.; Li, D.H.; Chen, Y.Q. Modified active disturbance rejection control design based on gain scheduling for selective catalytic reduction denitrification processes. *IEEE Trans. Ind. Electron.* **2024**, *71*, 16441–16451. [CrossRef]
20. Wang, Y.; Shi, G.J.; Wu, Z.L. Research on modified active disturbance rejection control and its engineering application for superheated steam temperature system. *Therm. Power Gener.* **2025**, *54*, 150–157. [CrossRef]
21. Mrabet, N.; Benzazah, C.; Mohssine, C.; Ahmed, E.a.; Driss, K.; Badr, R.; Ilyas, L. Enhancing wind energy conversion efficiency: A novel MPPT approach using P&O with ADRC controllers versus PI controllers with Kp and Ki optimization via genetic algorithm and ant colony optimization. *Clean. Energy Syst.* **2024**, *9*, 100159. [CrossRef]
22. Rerhrhaye, B.; Rerhrhaye, F.; Lahlouh, I.; El Akkary, A.; Sefiani, N.; Mrabet, N.; Khouili, D.; Ennaciri, Y.; El Martaoui, C. Proposal of an interleaved boost converter controlled by a nonlinear MPPT ADRC as the boost stage of a solar inverter connected to the hospital electrical network. *Clean. Energy Syst.* **2025**, *12*, 100222. [CrossRef]
23. Zhang, P.; Shi, Z.Y.; Yu, B.; Qi, H.J. Research on a sensorless ADRC vector control method for a permanent magnet synchronous motor based on the luenberger observer. *Processes* **2024**, *12*, 906. [CrossRef]
24. Dou, Z.L.; Zhang, C.Y.; Zhou, X.C.; Gao, D.; Liu, X.H. DDPG-ADRC-based load frequency control for multi-region power systems with renewable energy sources and energy storage equipment. *Energies* **2025**, *18*, 3610. [CrossRef]
25. Wu, Z.L.; Li, D.H.; Liu, Y.H.; Chen, Y.Q. Performance analysis of improved ADRCs for a class of high-order processes with verification on main steam pressure control. *IEEE Trans. Ind. Electron.* **2023**, *70*, 6180–6190. [CrossRef]
26. Zenon, Z.; Lech, D.; Jarosław, A. Design and assessment of ADRC-based autopilot for energy-efficient ship steering. *Energies* **2021**, *14*, 7937. [CrossRef]
27. Neria, M.R.; Ortega, G.O.; Ossaba, A.T.; Martinez, E.G.H.; González, A.L.; Tejada, J.C. Trajectory tracking of a 2-degrees-of-freedom serial flexible joint robot using an active disturbance rejection controller approach. *Mathematics* **2024**, *12*, 3989. [CrossRef]
28. Zong, H.Z.; Yang, Z.X.; Yu, X.; Zhang, J.H.; Ai, J.K.; Zhu, Q.X.; Wang, F.; Su, Q.; Xu, B. Active disturbance rejection control of hydraulic quadruped robots rotary joints for improved impact resistance. *Chin. J. Mech. Eng.* **2024**, *37*, 103. [CrossRef]

29. Lu, Q.L.; Sun, R.S.; Lu, Y. Output redefinition-based active disturbance rejection control for nonminimum phase hypersonic vehicles. *Aircr. Eng. Aerosp. Technol.* **2024**, *96*, 530–540. [CrossRef]
30. Huo, B.Y.; Wang, Y.A.; Zhang, Z.; Dong, A.Q.; Liu, Y.H. Multi-electrode coordinated upper limb rehabilitation motion control method based on ADRC. *J. Zhengzhou Univ. Sci.* **2025**, *46*, 1–10+18. [CrossRef]
31. Ye, Y.H.; Cheng, Y.; Zhou, F.; Lu, G.P. Optimization of active disturbance rejection controller for distillation process based on quantitative feedback theory. *Processes* **2025**, *13*, 1436. [CrossRef]
32. Zeng, Q.S.; Zhou, Y.S.; Tao, C.C.; Liu, Y.H. Active disturbance rejection robust hamiltonian tracking control of electrically driven manipulator. *J. Zhengzhou Univ. Sci.* **2022**, *43*, 1–7+15. [CrossRef]
33. Zhao, S.; Gao, Z.Q. Modified active disturbance rejection control for time-delay systems. *ISA Trans.* **2014**, *53*, 882–888. [CrossRef]
34. Zheng, Q.L.; Gao, Z.G. Predictive active disturbance rejection control for processes with time delay. *ISA Trans.* **2014**, *53*, 873–881. [CrossRef] [PubMed]
35. Wu, Z.L.; He, T.; Li, D.H.; Xue, Y.L.; Sun, L.; Sun, L.M. Superheated steam temperature control based on modified active disturbance rejection control. *Control Eng. Pract.* **2019**, *83*, 83–97. [CrossRef]
36. Fan, Y.S.; Xu, Z.G.; Cheng, L.J. Study of adaptive fuzzy control of boiler superheated steam temperature based on dynamic mechanism analysis. *Proc. CSEE* **1997**, *17*, 23–28. [CrossRef]
37. Zhao, C.Z.; Li, D.H. Control design for the SISO system with the unknown order and the unknown relative degree. *ISA Trans.* **2014**, *53*, 858–872. [CrossRef]
38. Song, X.D.; Zhao, Y.D.; Li, Z.H.; Song, J.C.; Wu, Z.L.; Guo, J.Z.; Zhang, J. A dual-loop modified active disturbance rejection control scheme for a high-purity distillation Column. *Processes* **2025**, *13*, 1359. [CrossRef]
39. Yan, S.B.; Li, J.J.; Zhang, X.D.; Shi, S.J.; Zheng, J.H. Improved modeling method of superheated steam in power plant. *J. Zhengzhou Univ. Sci.* **2012**, *33*, 55–58. [CrossRef]
40. Yang, X.L.; Yu, G.Q.; Zhang, T.H.; Cui, X.B. Control of superheated steam temperature system for wide load based on adaptive strategy. *Autom. Instrum.* **2025**, *40*, 32–38. [CrossRef]
41. Niu, H.M.; Yu, J.; Ding, C.F.; Wang, C.H.; Tian, B. Active disturbance rejection control over superheated steam temperature based on multi-objective particle swarm optimization. *Electr. Power* **2020**, *53*, 126–133. [CrossRef]

Disclaimer/Publisher's Note: The statements, opinions and data contained in all publications are solely those of the individual author(s) and contributor(s) and not of MDPI and/or the editor(s). MDPI and/or the editor(s) disclaim responsibility for any injury to people or property resulting from any ideas, methods, instructions or products referred to in the content.